

THE HYDROGEN EPOCH OF REIONIZATION ARRAY DISH II: CHARACTERIZATION OF SPECTRAL STRUCTURE WITH ELECTROMAGNETIC SIMULATIONS AND ITS SCIENCE IMPLICATIONS.

AARON EWALL-WICE^{1,2}, RICHARD BRADLEY^{3,4}, DAVID DEBOER⁵, JACQUELINE HEWITT^{1,2}, AARON PARSONS⁵, JAMES AGUIRRE⁶, ZAKI S. ALI⁵, CARINA CHENG⁵, ABRAHAM NEBEN^{1,2}, NIPANJANA PATRA⁵, NITHYANANDAN THYAGARAJAN⁷, MARIET VENTER⁸, JUDD BOWMAN⁶, ELOY DE LERA ACEDO⁹, ROGER DICKENSON³, PHILLIP DOOLITTLE³, DENNIS EGAN³, MIKE HEDRICK³, SAUL KOHN⁶, PATRICK SCHAFFNER³, JOHN SHELTON³, BENJAMIN SALIWANCHIK¹⁰, MAX TEGMARK^{1,2} H.A. TAYLOR³, RUSTY TAYLOR³, BUTCH WIRT³,

Draft version February 17, 2016

ABSTRACT

We use time domain electromagnetic simulations to assess the spectral characteristics of the dish antenna for the Hydrogen Epoch of Reionization Array (HERA). These simulations are part of a multi-faceted campaign to determine whether the dish design is suitable for obtaining a detection of redshifted 21 cm emission from the Epoch of Reionization. Our simulations show the existence of reflections in some regions of the 100-200 MHz bandpass with an amplitude of ≈ -35 dB at 100 ns which can lead to some loss of measurable modes and a modest reduction in sensitivity. Even in the presence of this structure, we find that the spectral response of the dish is sufficiently smooth for proven foreground isolation methods such as delay filtering to contain foreground emission at line of sight wave numbers below $k_{\parallel} = 0.15 - 0.23 \text{ hMpc}^{-1}$. Incorporating these results into a Fisher Matrix analysis, we find that the spectral structure observed in our simulations has only a small effect on the overall constraints on the astrophysics of reionization that HERA will achieve, allowing it to serve as a benchmark for the design of future instruments.

1. INTRODUCTION

Observations of the redshifted 21 cm radiation from neutral hydrogen in the intergalactic medium (IGM) have the potential to illuminate the hitherto unobserved *dark ages* and *cosmic dawn*, revolutionizing our understanding of the first UV and X-ray sources in the universe and how their properties influenced galactic evolution (see Furlanetto et al. (2006), Morales & Wyithe (2010), and Pritchard & Loeb (2012) for reviews). Two major experimental endeavors are underway to detect the 21 cm signal, with most focusing on the Epoch of Reionization (EoR) in which UV photons from early galaxies transformed the hydrogen in the universe from neutral to ionized. The first involves measuring the sky-averaged global signal and is being pursued by experiments such as EDGES (Bowman & Rogers 2010), LEDA (Greenhill & Bernardi 2012; Bernardi et al. 2015), DARE (Burns et al. 2012), SciHi (Voytek et al. 2014), and BIGHORNS (Sokolowski et al. 2015) either in their planning stages or already taking data. The second attempts to observe spatial fluctuations in the 21 cm emission using radio interferometers. A first generation of such experiments are currently taking data in an attempt to make a first statistical detection of the power spectrum of 21 cm bright-

ness temperature fluctuations. These include the Giant Metrewave Telescope (GMRT) (Paciga et al. 2013), the Low Frequency ARray (LOFAR), (van Haarlem et al. 2013), the Murchison Widefield Array (Tingay et al. 2013), the MIT Epoch of Reionization Experiment (MITEoR) (Zheng et al. 2013), and the Precision Array for Probing the Epoch of Reionization (PAPER) (Parsons et al. 2010). Already, many of these experiments are beginning to yield upper limits on the 21 cm signal (Dillon et al. 2013; Parsons et al. 2014; Jacobs et al. 2015; Dillon et al. 2015a) and significant scientific results. The most stringent measurement of $\approx 500 \text{ mK}^2$ (Ali et al. 2015) is able to rule out number of scenarios in which the intergalactic medium received little or no heating from X-rays (Pober et al. 2015; Greig et al. 2015b).

The primary challenge to obtaining a high redshift detection of the cosmological signal through both of these methods is the existence of foregrounds that are $\sim 10^5 - 10^6$ times brighter (Bernardi et al. 2009; Pober et al. 2013a; Dillon et al. 2014). While requiring much greater sensitivity than global-signal experiments, interferometers have the advantage that spectrally smooth foregrounds are naturally contained to a finite region of Fourier space, corresponding to large line of sight scales, known as the *wedge* (Datta et al. 2010; Vedantham et al. 2012; Parsons et al. 2012; Thyagarajan et al. 2013; Liu et al. 2014a,b). Since the location of each foreground on the sky determines its position in the wedge, with sources near the horizon being introduced at line of sight scales closest to the *EoR window*, the angular response of an instruments beam pattern has significant implications on the amount of side-lobe power that is leaked into the EoR window (Thyagarajan et al. 2015b,a; Pober et al. 2016).

Beyond leakage from wedge side-lobes, any structure in the frequency response of the instrument is imprinted on the foregrounds and has the potential to leak power into

¹ MIT Kavli Institute for Cosmological Physics

² MIT Dept. of Physics

³ National Radio Astronomy Obs., Charlottesville VA

⁴ Dept. of Astronomy, U. Virginia, Charlottesville VA

⁵ Astronomy Dept. U. California, Berkeley CA

⁶ Dept. of Physics and Astronomy, University of Pennsylvania, Philadelphia, PA

⁷ School of Earth and Space Exploration, Arizona State U. Tempe AZ

⁸ Cavendish Laboratory, University of Cambridge, Cambridge, UK

⁹ SKA South Africa, Cape Town, SA

¹⁰ University of KwaZulu-Natal, Durban, SA

the EoR window at small line of sight scales, masking the signal. Indeed, sub-percent spectral features in the analogue and digital signal chains on the initial build-out of the MWA are proving to be a significant calibration challenge (Dillon et al. 2015b; Ewall-Wice et al. in review; Beardsley et al. in preparation).

While, in principle, spectral structure in the bandpass of the instrument may be removed in calibration, it is being investigated whether any mismodeling of emission and the primary beam will mix the significant spectral structure introduced by the wedge on long baselines into short ones, masking the signal entirely (Barry et al. in preparation). While redundant calibration (Wieringa 1992; Liu et al. 2010; Zheng et al. 2014) is able to solve for gains that are primarily independent of a detailed model of the sky, antenna elements with significant direction dependent chromaticity that varies from element to element might break the assumptions of redundancy that such calibration relies upon and pose a significant obstacle. Because of our limited knowledge of foregrounds at low frequency and the fidelity of calibration algorithms, it is imperative to design experiments whose band-passes are as devoid of spectral structure as possible.

Drawing off of the lessons of the PAPER, MWA, and MITEoR experiments, the Hydrogen Epoch of Reionization Array (HERA) (Poher et al. 2014; DeBoer et al. submitted) is a next generation 21 cm experiment designed to achieve a two-orders of magnitude improvement in sensitivity over current experiments which will allow it to make a robust detection of the 21 cm power spectrum during the EoR. Much of this sensitivity increase is enabled by moving the collecting area of the instrument into baselines that are located primarily inside of the EoR window and a switch from PAPER’s skirted dipoles and the MWA’s phased dipole arrays to an antenna element that consists of a feed suspended over a large reflecting parabolic dish. A central requirement for HERA’s dish design is that the antenna have a response that is sufficiently smooth in frequency and centralized enough in its angular response that it leaves the EoR window free of the side-lobe contamination observed in (Thyagarajan et al. 2015b,a; Poher et al. 2016). Central to increasing the collecting area of each element on HERA is a switch from dipoles (used by the MWA and PAPER) to feeds suspended over large 14 m diameter parabolic dishes. In Fig. 1 we show one of the initial 19 dishes currently being deployed in South Africa at the same site as PAPER whose antenna we also show at the top of the figure.

This paper and its companions (Neben et al. 2016; Patra et al. in preparation; Thyagarajan et al. submitted) describe a multi-pronged campaign to assess whether the HERA dish meets the requirements for isolating foregrounds within the wedge and leaving the EoR window clean. We accomplish this by establishing antenna specifications with simulations of foregrounds (Thyagarajan et al. submitted) and verifying that the HERA primary antenna element meets these specifications with reflectometry (Patra et al. in preparation) and ORBCOMM beam mapping (Neben et al. 2016). In this work, we present the results of time-domain electromagnetic simulations that are intended to predict the degree of spectral structure in the HERA dish, assess the impact of this spectral structure on the leakage of foregrounds into the EoR window, and to verify the reflectometry mea-

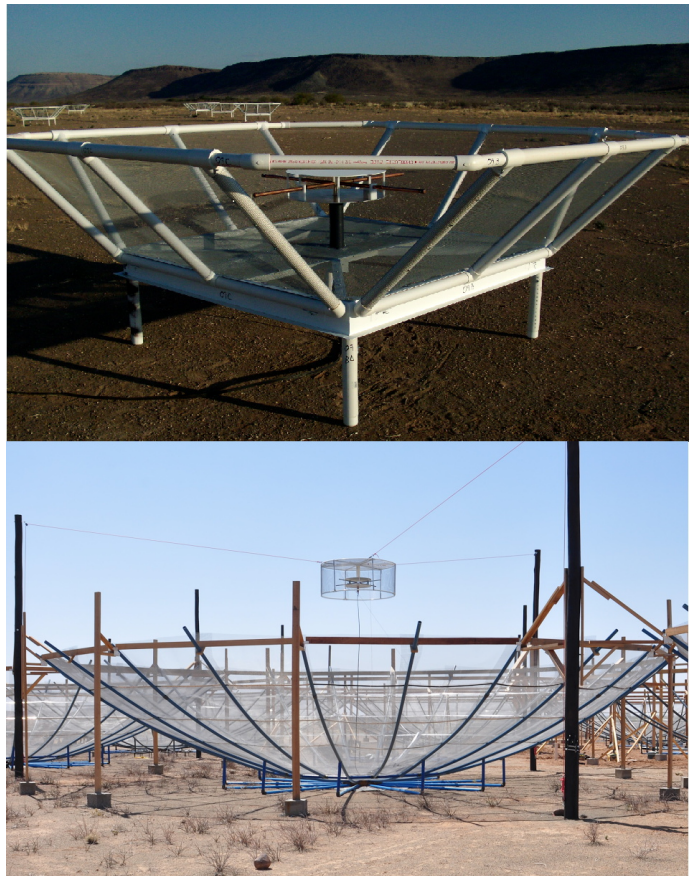


FIG. 1.— The HERA antenna element (bottom) uses a parabolic dish to achieve an order of magnitude increase in collecting area over the PAPER antenna (top). The sleeved dipole in the center of the PAPER backplane is identical to the sleeved dipole being suspended under the cylindrical skirt over the vertex of the HERA dish. The suspended feed arrangement has the potential to introduce intra-antenna reflections which we explore in this work.

surements taken in the field.

This paper is organized as follows. In § 2 we lay out our analytic framework and describe the impact of reflections and spectral structure on foreground leakage in delay-transform power spectra. In § 3 we describe our time-domain electromagnetic simulations of the HERA dish element and how we extract the voltage response function. In § 4 we describe the results and verify our simulation framework by comparing its prediction of the S_{11} parameter of the HERA dish to direct field measurements described in (Patra et al. in preparation). In § 5 we apply our electromagnetic simulation results to a foreground model to determine the extent that the HERA dish’s chromatic structure pollutes the EoR window and the impact on HERA’s ability to constrain reionization parameters. We summarize our conclusions in § 6.

2. THE IMPACT OF REFLECTIONS ON DELAY-TRANSFORM POWER SPECTRA

In this section, we show how reflections in the analogue signal path of an antenna lead to foreground contamination of the EoR window. Intuitively, any reflections in the signal path introduce sinusoidal ripples in the frequency dependent gain of the instrument. Since time delay is the Fourier dual to frequency, reflections with larger delays introduce ripples with shorter periods. Isolation of the 21 cm signal from foregrounds that are over

four orders of magnitude brighter depends critically on their smoothness. Any sinusoidal frequency structure introduced by the reflections will cause these foregrounds to mimic and swamp the signal unless they are brought below a level similar to the ratio between the foregrounds and the signal itself. A simple equation describing the effect of direction independent reflections in the signal chain downstream of the feed has been derived in Ewall-Wice et al. (in review). We now extend this analysis by considering the direction dependent reflections that can occur within the antenna element. We start by denoting the electric field of radiation arriving from direction ℓ at the i^{th} antenna element at position \mathbf{x}_i and time $t_i = t + \hat{\mathbf{r}} \cdot \mathbf{x}_i/c \equiv t + \tau_i$ as $\tilde{s}(\hat{\mathbf{r}}, \mathbf{x}_i, t_i)$.

Reflections within the signal chain of each antenna are most generally described by a direction dependent reflection coefficient, $\tilde{r}_i(\hat{\mathbf{r}}, \tau)$. Its effect is to add the signal to itself multiplied by \tilde{r}_i and delayed by τ . The voltage signal measured at the i^{th} antenna element, \tilde{v}_i , is the integral over solid angle of the electric fields arriving from all directions. The presence of reflections introduces a convolution of the electric field entering the antenna (delayed by τ_i) with $\tilde{r}_i(\hat{\mathbf{r}}, \tau)$:

$$\tilde{v}_i(t) = \int d\Omega \int d\tau \tilde{r}_i(\hat{\mathbf{r}}, \tau) \tilde{s}(\hat{\mathbf{r}}, t - \tau_i - \tau). \quad (1)$$

Applying the Fourier convolution theorem, the Fourier transform of this equation gives $v_i(\omega)$ as the simple angular integral of the product of $s_i(\hat{\mathbf{r}}, \omega)$ and $r_i(\hat{\mathbf{r}}, \omega)$, where ω is the angular frequency of electromagnetic radiation.

$$v_i(\omega) = \int d\Omega r_i(\hat{\mathbf{r}}, \omega) s(\hat{\mathbf{r}}, \omega) e^{-i\omega\tau_i}. \quad (2)$$

The correlator of a radio interferometer records the time-averaged product of the Fourier transformed voltage streams of the i^{th} and j^{th} antennas. The time averaged product of the Fourier transform between the two antennas is

$$\begin{aligned} V'_{ij}(\omega) &= \langle v_i(\omega) v_j^*(\omega) \rangle_t \\ &= \int d\Omega r_i(\hat{\mathbf{r}}, \omega) r_j^*(\hat{\mathbf{r}}, \omega) I(\hat{\mathbf{r}}, \omega) e^{-i\omega\Delta\tau_{ij}} \\ &= \int d\Omega r_i(\hat{\mathbf{r}}, \omega) r_j^*(\hat{\mathbf{r}}, \omega) I(\hat{\mathbf{r}}, \omega) e^{-i\omega\mathbf{b}_{ij} \cdot \hat{\mathbf{r}}/c}, \end{aligned} \quad (3)$$

where $\Delta\tau_{ij} = \tau_i - \tau_j = (\mathbf{x}_i - \mathbf{x}_j) \cdot \hat{\mathbf{r}}/c$, $I(\hat{\mathbf{r}}, \omega) = \langle |s(\hat{\mathbf{r}}, \omega)|^2 \rangle_t$, and $\mathbf{b}_{ij} = (\mathbf{x}_i - \mathbf{x}_j)$. Here, we have invoked the fact that electromagnetic waves arriving from different directions are incoherent. This equation leaves us with the familiar interferometry equation (Thompson et al. 1986), allowing us to see that $r_i(\hat{\mathbf{r}}, \omega)$ equivalent to the voltage beam of the antenna. Setting a specification on reflections is hence equivalent to setting a specification on the spectral smoothness of the antenna's voltage beam.

In order to filter spectrally smooth foregrounds from the signal, numerous experiments expect to employ the *delay transform* over frequency, defined as (Parsons et al. 2012)

$$\tilde{V}_{ij}(\tau) = \frac{1}{2\pi} \int d\omega V_{ij}(\omega) e^{i\omega\tau}. \quad (4)$$

Applying this to equation 3, we obtain

$$\tilde{V}_{ij}(\tau) = \frac{1}{2\pi} \int d\Omega \int d\omega r_i(\hat{\mathbf{r}}, \omega) r_j^*(\hat{\mathbf{r}}, \omega) I(\hat{\mathbf{r}}, \omega) e^{-i\omega(\mathbf{b}_{ij} \cdot \hat{\mathbf{r}}/c - \tau)}. \quad (5)$$

Let's examine the quantity within the angular integral. We see that each source located at $\hat{\mathbf{r}}$ on the sky is mapped to a line $\tau = \mathbf{b}_{ij} \cdot \hat{\mathbf{r}}/c$, resulting in the much discussed "wedge" (Datta et al. 2010; Vedantham et al. 2012; Parsons et al. 2012; Morales et al. 2012; Thyagarajan et al. 2013; Liu et al. 2014a,b). The presence of the frequency dependent beam causes each source line to be convolved in delay with the direction dependent kernel,

$$\tilde{R}_{ij}(\hat{\mathbf{r}}, \tau) = \int d\tau' \tilde{r}_i(\hat{\mathbf{r}}, \tau - \tau') \tilde{r}_j^*(\hat{\mathbf{r}}, -\tau'), \quad (6)$$

which is the convolution of the delay response of the voltage beam of antenna i with the time-reversed complex conjugate of voltage beam of antenna j . In the remainder of this paper, we will often refer to \tilde{R} as the *power kernel* applied to a visibility. Note that this is not equal to the convolution of the voltage response with its complex conjugate, which would lead to foreground power only being bled out to positive delays. We demonstrate the effect of foreground smearing in Fig. 2 for a simple model with only three sources. Without reflections, the sources would form lines intersecting zero in the two dimensional space with the baseline length, b on the x-axis and the delay, τ on the y-axis. With the reflections, the sources are smeared out, leading to supra-horizon emission. For the sake of simplicity, we now consider the case where the beam can be factored into angular and frequency independent components, $r_i(\hat{\mathbf{r}}, f) = g_i(f) a_i(\hat{\mathbf{r}})$. For such a case, every line in Fig. 2 would be convolved with the same delay dependent shape, normalized to the gain of $a_i(\hat{\mathbf{r}})$. In this situation, we have

$$\tilde{V}_{ij}(\tau) = \int d\tau' \int d\tau'' \tilde{g}_i(\tau' - \tau'') \tilde{g}_j^*(-\tau'') \tilde{V}_{ij}^a(\tau - \tau'), \quad (7)$$

where V_{ij}^a is the visibility for the achromatic voltage pattern, $a_i(\hat{\mathbf{r}})$. We can gain further insight into the behavior of the delay kernel arising from chromaticity by assuming that $\tilde{g}_i(\tau = 0) \gg \tilde{g}_i(\tau > 0)$, which should be the case at large delays for the smooth bandpasses our instruments are designed to have.

$$\begin{aligned} \tilde{V}_{ij}(\tau) &\approx \tilde{g}_i(0) \int d\tau' \tilde{g}_j^*(-\tau') \tilde{V}_{ij}^a(\tau - \tau') \\ &\quad + \tilde{g}_j^*(0) \int d\tau' \tilde{g}_i(\tau') \tilde{V}_{ij}^a(\tau - \tau'). \end{aligned} \quad (8)$$

Hence, to first order, the impact of reflections is to convolve the delay-transformed visibility with the voltage beam of the instrument. This may be a somewhat un-intuitive result since naive dimensional analysis might predict that the power-kernel is proportional to the square of the delay-response. This linear falloff coupled with the enormous dynamic range between foregrounds and signal puts exquisite requirements on the smoothness of the beam, requiring that it fall five to six orders of magnitude in the regions of delay space that we want to measure the signal.

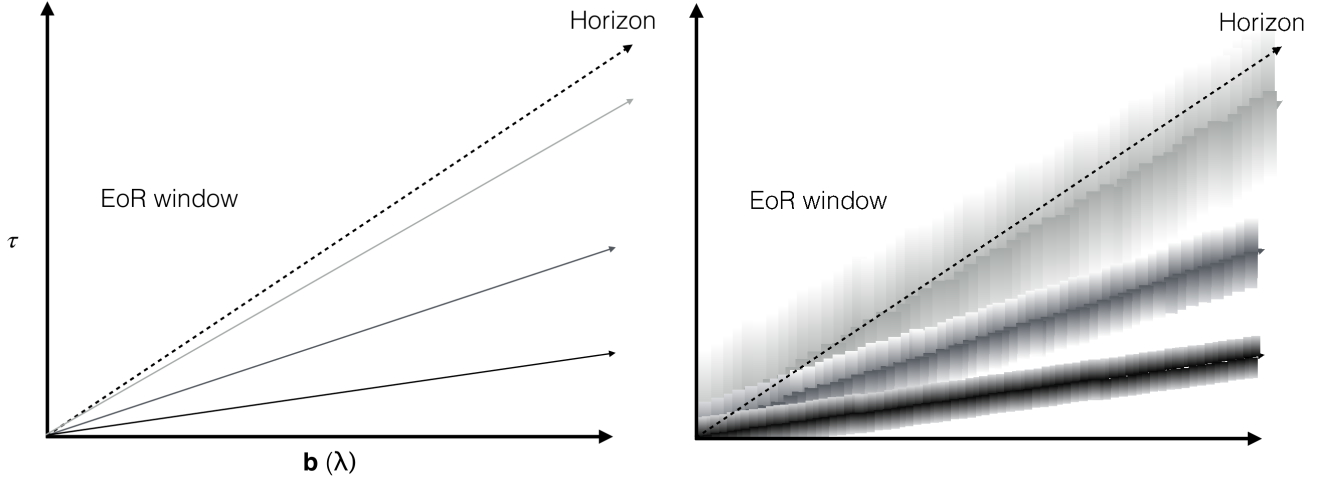


FIG. 2.— A cartoon demonstration of the impact on foregrounds of the frequency dependent beam. Left: The location of three sources in delay space assuming a frequency independent beam (no reflections in the antenna element). Right: the presence of chromaticity due to reflections in the antenna smears the source in delay with the kernel given by equation 6. Since the frequency response of the dish is a function of direction on the sky, the shape of the delay kernel is different for each source line. We see that this smearing can lead to substantial supra-horizon emission.

3. ELECTROMAGNETIC SIMULATIONS OF THE HERA DISH ELEMENT

Having formally derived the impact of analogue reflections on foreground visibilities, we are now in a position to investigate their existence in the HERA dish. In this section, we describe the setup and parameters of our simulations (§ 3.1), and how we extract the voltage response function of the dish (§ 3.2).

3.1. The Simulations

The time-dependent electromagnetic behavior of the antenna was modeled using Microwave Studio, a commercial numerical simulation package produced by Computer Simulation Technology (CST). The model consists of an idealized 14 m diameter paraboloid reflector with a feed structure placed at the focus (4.5 m above the surface). The feed was a dual linear polarized sleeved dipole identical to that used as an element of PAPER but with a cylindrical skirt used in place of the angled planar reflectors. The dipole arms were modeled as copper tubing and aluminum was assigned to the disks and reflector surfaces. For simulation, the entire model was encapsulated in vacuum dielectric with radiative boundaries and discrete ports of $125\,\Omega$ impedance were defined at the terminals of the orthogonal dipoles. The simulated is conducted in a box encapsulating the dish geometry plus three wavelengths (at 150 MHz) on all sides with open boundary conditions.

Microwave Studio divides the model into approximately 94 million discrete hexahedral cells where the field is calculated over time using Finite Integration Technique incorporating the Perfect Boundary Approximation¹¹ (Workflow and Solver Overflow Document, CST Microwave Studio, 2015, Chapter 3.) in response to a 100-200 MHz broadband pulse of about 40 ns in duration. The model was excited in two ways: 1) via a E-W

¹¹ This proprietary technique is used by CST to reduce the number of simulation cells and should not be confused with PEC periodic boundary conditions.

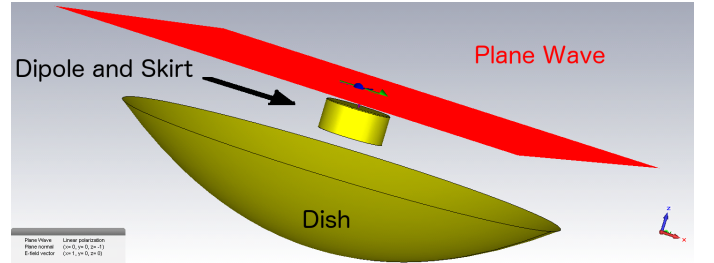


FIG. 3.— A rendering of our simulation setup at $t = 0$. The plane wave is started just above the feed (red plane).

polarized plane wave entering the model along the bore sight, and 2) from one of the discrete terminals (whose analysis we focus on in § 4.3). The voltage responses at the terminals are monitored for these two cases over a duration of 500 ns as the excitation pulse travels throughout the model.

In Fig. 3 we show the geometry of the electromagnetic simulation. A 150 MHz plane wave with a Gaussian envelope is initialized above the dish vertex traveling in the $-z$ direction. It is reflected by the dish before entering the dipole feed, hidden below the cylindrical skirt in this figure. We record the electric field voltage of the plane wave at the feed output terminals as a function of time, plotted as a red line in Fig. 4 along with the output voltage at the terminals for the feed polarized parallel to the plane wave (black line). The delay between the primary envelopes of the plane wave and the voltage output of the feed is ≈ 30 ns which corresponds to the round trip travel time from the feed to the dish vertex and back. However, while the input plane wave, modulated by a gaussian, falls off rapidly and dies off after the first ≈ 20 ns after its peak, we see that the voltage output decays far more slowly due to reflections within the dish-feed structure. We are able to get a qualitative feel for the amplitude of the reflections by inspecting the falloff of the time domain voltage response and see that after 60 ns it reaches ≈ -25 dB.

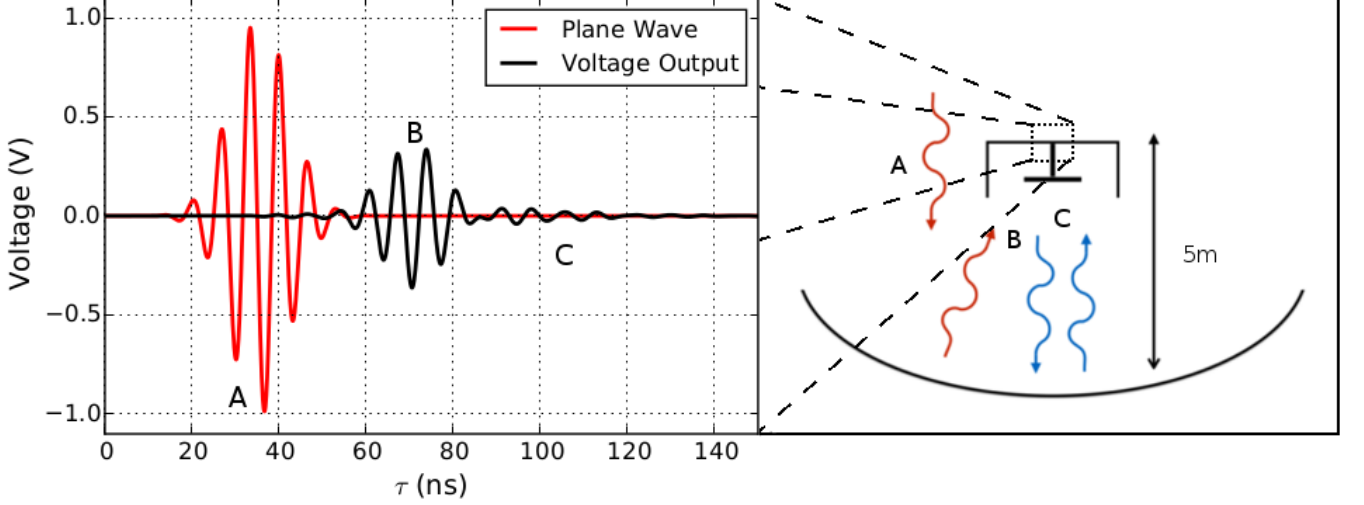


FIG. 4.— An illustration of our simulation products and their origin in the HERA antenna geometry. A plane wave is injected from above the feed. The electric field of the plane wave at the feed terminals (red line) along with the voltage output is recorded (black line). The feed in our simulation is situated 5 m above the bottom of the dish, hence there is a ≈ 30 ns delay between when the plane wave passes the terminal for the first time (A) and when it is first absorbed in the dipole (B), leading to the voltage response. Of concern to 21 cm experiments are the subsequent reflections between the feed and the dish (C) which can lead to large delay contamination of the EoR window.

3.2. Deconvolving the Response Function

We can do much better than this. From equation 1, we know that the voltage output results from the convolution of the plane wave input with the voltage gain of the antenna. Since we know the input wave, a straightforward application of the Fourier convolution theorem allows us to determine the voltage response.

Since our simulation is sampled in finite time steps, we will adopt discretized notation for this section. In particular, our simulation consists of N samples, evenly spaced by $d\tau$ at times $\tau_n = n \times d\tau$. We denote the output voltage at the feed terminals at time τ_n as \tilde{v}_n . Rewriting the convolution in equation 1 in discrete notation, we have

$$\tilde{v}_n(\mathbf{k}) = \sum_m \tilde{r}_m(\mathbf{r}) \tilde{s}_{n-m}(\mathbf{r}). \quad (9)$$

We may undo this convolution by taking a discrete Fourier transform (DFT) of both $\tilde{\mathbf{v}}$ and $\tilde{\mathbf{s}}$ in time, dividing them in Fourier space, and taking an inverse DFT back. Symbolically,

$$\tilde{r}(\mathbf{r}) = \mathcal{F}^{-1} \left[\frac{\mathcal{F}\tilde{\mathbf{v}}(\mathbf{r})}{\mathcal{F}\tilde{\mathbf{s}}(\mathbf{r})} \right], \quad (10)$$

where \mathcal{F} is the Fourier transform matrix for a 1d vector of length N .

$$\mathcal{F}_{mn} = e^{-2\pi i m n / N}. \quad (11)$$

In Fig. 5 we show the amplitude of the Fourier transform of our Gaussian input, centered at 150 MHz along with the voltage response. Since our input only has support between ≈ 20 and 280 MHz, the direct ratio of our voltage response and input wave is dominated by numerical noise outside of this range. We eliminate these artifacts by multiplying our ratio by a Blackman-Harris window between 100 MHz and 200 MHz and set our estimate to zero elsewhere. From a physical standpoint, this is sensible since 21 cm experiments only observe a limited bandwidth. PAPER's correlator, which will initially serve as

the HERA backend samples over a 100 MHz instantaneous frequency interval. Hence analogue filtering is applied to limit the incoming signal within this range to prevent aliasing.

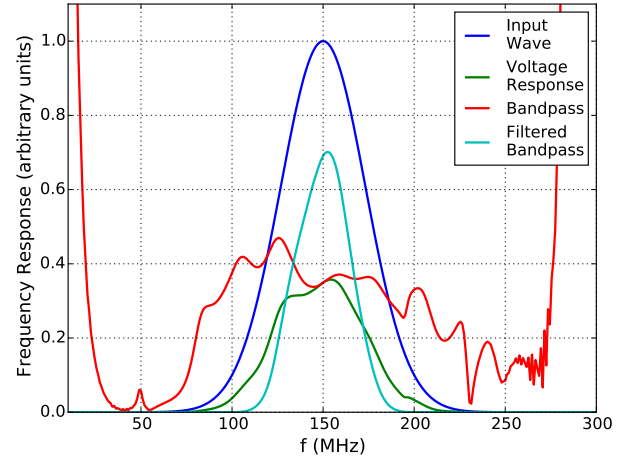


FIG. 5.— The absolute value of the Fourier transform of the voltage output from our dish (green line) and the input wave (blue line), normalized to the amplitude of the input wave at 150 MHz. The ratio between input and output is plotted as a red line. Since our input is limited to frequencies between ≈ 20 and 280 MHz, there are significant numerical artifacts in the ratio that causes divergence towards the plot edges. To eliminate this noise, we multiply by a Blackman-Harris window between 100 and 200 MHz and set our estimate to zero elsewhere (cyan line).

4. SIMULATION RESULTS

We now discuss the results of our simulations. In particular, we focus on the time-domain die off of the voltage response and the resulting power kernel (§ 4.1), comparing it to an identical time-domain simulation of the skirted dipole antenna used by PAPER. In § 4.2 we inves-

tigate the dependence of the power kernel on frequency to determine whether specific parts of the HERA bandpass are more affected by reflections than others. Finally, in § 4.3 we verify our simulation framework by comparing a separate time domain simulation of S_{11} of the HERA dish to a direct field measurement with a vector network analyzer (VNA).

4.1. The Time Domain Response of the HERA Dish

Applying equation 10 to our simulation, we obtain estimates of the time-domain voltage response of the HERA dish towards zenith which we plot in Fig. 6. We also conduct a time-domain simulation of the voltage output in response to an identical input plane wave for the skirted dipole PAPER antenna (pictured above the HERA dish in Fig. 1) in order to determine whether the presence of the parabolic dish introduces reflections and spectral structure in excess of previous successful antenna designs¹². We inspect the absolute value of \tilde{v} for both the PAPER and HERA antennas in Fig. 6. Since non-zero values of \tilde{v} at negative delays violates causality, we assume such features are sourced by numerical artifacts such as side-lobes and/or numerical precision noise which sets a limit of ≈ -60 dB on the dynamic range of our method. An obvious difference between the two curves is a knee in the HERA gain at ≈ 120 ns that is not present in PAPER, leading to an increase in gain of nearly 20 dB at 200 ns. This is an important and perhaps not unsurprising finding: in moving from a skirted dipole to a reflecting dish to increase collecting area and overall sensitivity we have added additional chromatic structure from reflections between the dish and the feed.

Our next step is to compute the power kernel, \tilde{R} , given by equation 6. Since structure at negative delays in our estimate of \tilde{v} is due to numerical artifacts and sidelobes, we set the voltage response to zero at $\tau < 0$ before performing a convolution with its time-reverse complex conjugate. In Fig. 7 we show the resulting power kernel for PAPER and HERA. Since both voltage gains drop rapidly with increasing delay, the approximation in equation 8 holds quiet well and we see that the kernels fall off at a rate similar to the response function itself.

4.2. The Delay Response of Subbands

Because the 21 cm brightness temperature fluctuations evolve over redshift intervals of $\Delta z \gtrsim 0.5$ (Zaldarriaga et al. 2004), experiments will sub-divide their bands into ≈ 10 MHz intervals for power spectrum estimates at multiple redshifts. Thus the localization of reflections within the HERA band will determine whether all or only a subset of redshifts are affected. To determine whether the reflections are localized in frequency, we compute the voltage delay response and power kernel for three different subbands: 100 – 130 MHz, 130 – 160 MHz, and 160 – 190 MHz. In order to maintain decent resolution of the kernel itself, we use frequency ranges that are several times larger than the actual subbands that will be used for EoR power spectrum estimation (≈ 10 MHz). The resulting power kernels are plotted in Fig. 8. The central lobe of the subband kernels is significantly wider due to the the wider window functions incurred by the reduced

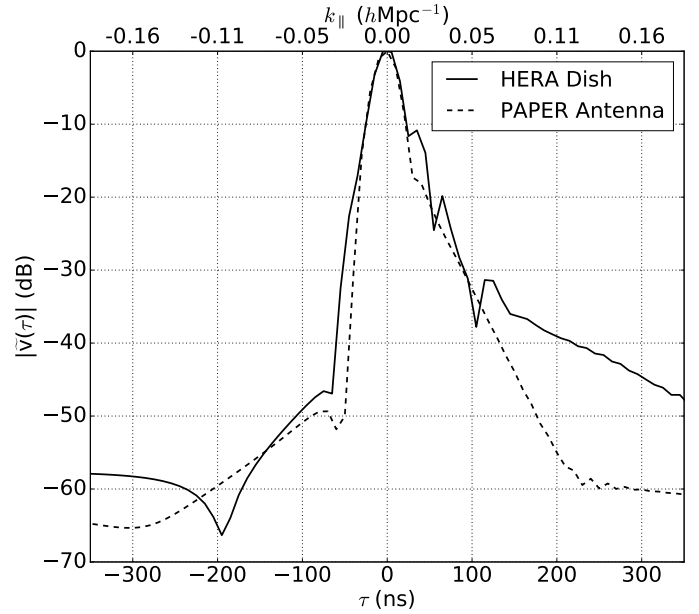


FIG. 6.— The Fourier transform of the simulated voltage response of the HERA Dish (solid black line) and the PAPER antenna element (dashed black line). Reflections in the HERA dish element lead to significantly enhanced power above ~ 50 ns. Since negative delays should be devoid of signal, they allow us to determine the dynamic range of our simulations which have a numerical noise/sidelobes floor of -60 dB.

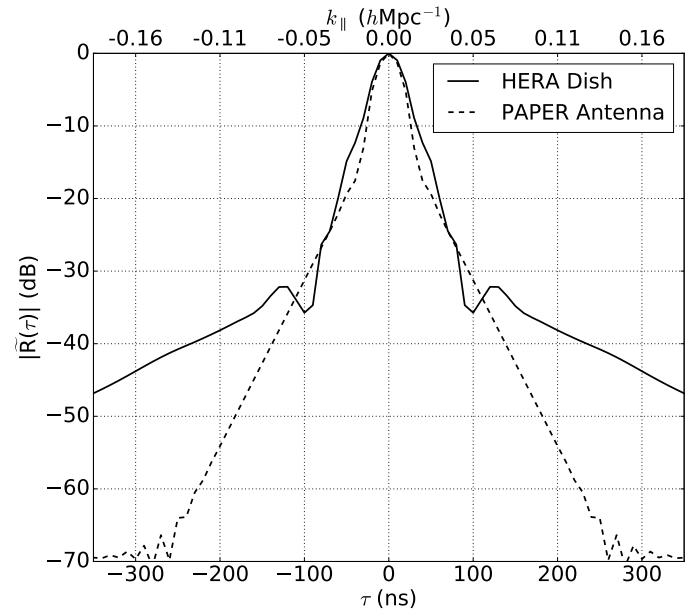


FIG. 7.— The absolute value of the power kernel for the HERA dish (solid black line) and for the PAPER antenna element (dashed black line) calculated using equation 6. While an antenna can only physically have a voltage response at positive delays, the delay kernel is formed from the convolution of one antenna with the time reversed conjugate response function of the other. Hence, the power kernel for two identical antennas will have $\tilde{R}(\tau) = \tilde{R}^*(-\tau)$.

bandwidth. However, the shallow long-term falloff is only visible within the central 130 – 160 MHz band, indicating that long term reflections are isolated around 150 MHz.

To further illustrate the observed isolation of fine frequency structure in the center of the bandpass and to verify that our observations are not an artifact of our

¹² To date, PAPER has produced the most stringent limits on the 21 cm power spectrum leading us to use its design as a standard

reduction of the simulation outputs, we observe the reflections in frequency space by fitting 10 MHz intervals of the absolute value of the simulated gains to a sixth order polynomial and inspecting the residuals in Fig. 9. We find that the gain residuals on the sixth order fit are an order of magnitude greater on the 145 – 155 MHz subband than any other frequency interval.

We note that the termination impedance used in our simulations is 125Ω to which the feed is better matched towards its edges. Termination by a low-noise amplifier (LNA) as is the case in an actual measurement could change this situation dramatically, leading to the reflections being present across the entire band. We therefore consider the existence of the reflections across the entire 100 MHz bandpass as a realistic possibility.

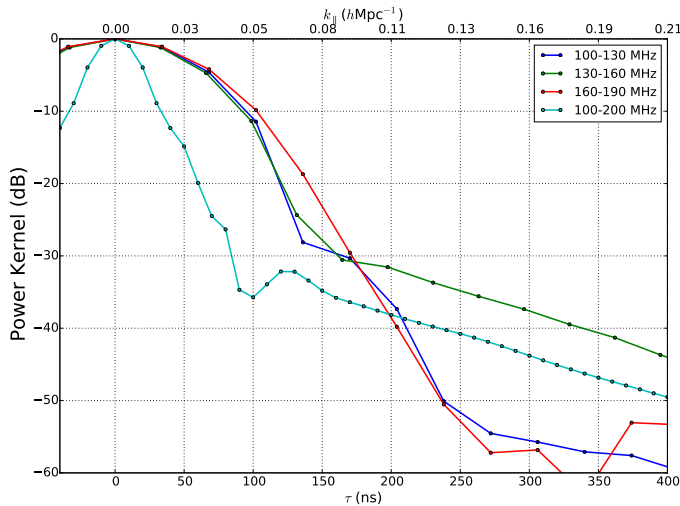


FIG. 8.— The power kernel for the three subbands discussed in § 4.2 along with the kernel for the full bandwidth response function. While the long term falloff from reflections is prominent between 130 – 160 MHz, it appears at a much lower level in the other two subbands which fall below the central subband by ~ 20 dB at ~ 300 ns. k_{\parallel} values for each delay are computed at 150 MHz. The wider central lobe below 150 ns for the subband gains is due to the lower delay resolution from the smaller bandwidth.

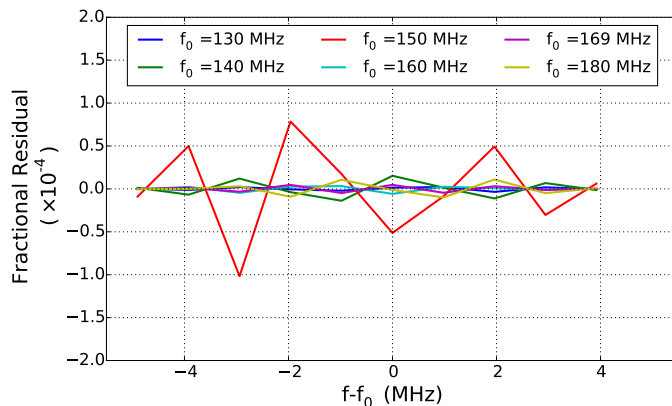


FIG. 9.— Residuals on the absolute value of the gain over several subbands after fitting to a sixth order polynomial. Consistent with our findings in Fig. 8, the fine frequency residuals in the 145–155 MHz subband are over an order of magnitude greater than those in the other subbands.

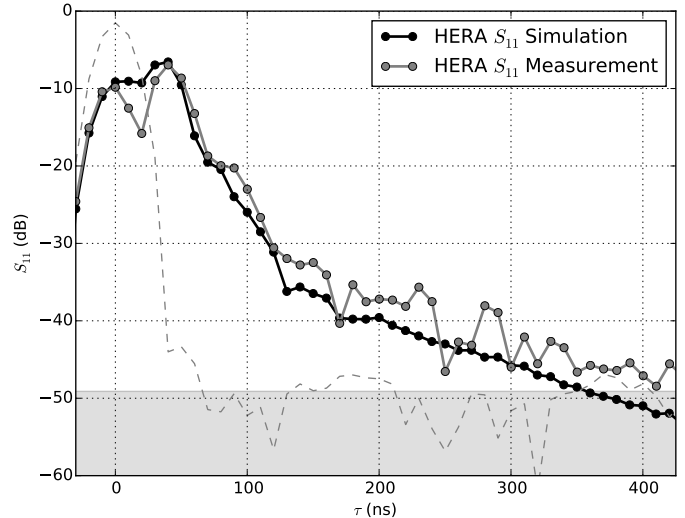


FIG. 10.— A comparison between time-domain simulations (black line) and measurements (grey line) of S_{11} for the HERA dish. We also show an S_{11} measurement with the cables leading from the VNA to the feed terminated by an open circuit which allows us to probe the dynamic range of the measurement. We use the standard deviation of the open measurement (grey dashed line) between 200 and 400 ns as our systematic floor (grey shaded region). We find very good agreement between our S_{11} measurement and the simulation, validating the predictions of our simulations. Both the simulations and measurements in this figure were derived from delay transforms over 100 MHz.

4.3. Verifying Our Framework with S_{11} Measurements and Simulations

We now assess the accuracy of our time-domain simulation framework by comparing simulations to measurements of the S_{11} parameter of the HERA dish. Up until now, our simulations have derived the voltage response of the dish using simulations of an incoming plane wave as is the case for radio signals arriving from objects at cosmological distances. It is possible to probe the gain of the dish using objects in the far field such as known radio sources (Thyagarajan et al. 2011; Pober et al. 2012; Colegate et al. 2015) or constellations of ORBCOMM satellites (Neben et al. 2015, 2016). However natural radio sources are too weak to probe the dish response at the $< 10^{-4}$ level necessary to verify our simulations and the ORBCOMM technique can only be used to map the gain at the 137 MHz ORBCOMM transmission frequency. Work is currently underway to use broad-band transmitters flown into the far field of the dish by drones (Jacobs et al. in preparation) but this system is still under development. Reflectometry of the dish with a VNA is a straightforward alternative used in Patra et al. (in preparation) to estimate the gains directly. Rather than comparing their estimate of the gain with our predicted gains (which is done in their paper), we set up a time domain simulation to compute the S_{11} parameter of HERA antenna and compare it to direct S_{11} measurements.

S_{11} refers to the complex ratio between a voltage signal transmitted into the feed terminals and the voltage reflected back as a function of frequency, $S_{11}(f) \equiv v_{\text{trans}}(f)/v_{\text{recv}}(f)$. We measure S_{11} of a prototype HERA dish at the National Radio Astronomy Observatory Green Bank facility using an Agilent 8753D VNA. The VNA is connected to the antenna’s balanced feed

terminal via a 30.5 m length of RG-8X-LL coaxial cable and M/A Com HH-128 180 degree hybrid junction. The VNA was calibrated at the balanced end of the hybrid junction using a set of termination standards having SMA connectors. A small adapter from SMA to the post terminals on the feed was not included in the calibration. The VNA excites the terminals with a band-limited (100-200 MHz) pulse, and the complex reflected voltage at the calibration plane is measured as a function of frequency. The reflection for the case of open terminals was measured to confirm the dynamic range and resolution of the measurement. While our simulations are terminated with an impedance of $125\ \Omega$, the VNA measurements are terminated at $100\ \Omega$.

Because S_{11} is defined as a ratio in the frequency domain in a form identical to our voltage gains, we may run time-domain simulations similar to those described in § 3.1 except rather than simulating an incoming plane wave, we simulate the excitation of the feed terminals by a delta-gap impedance port and record output voltage as a function of time. We calculate S_{11} from the simulation in the same manner that we obtained \tilde{r} using equation 10 with \tilde{v}_{recv} taking the place of \tilde{v} in the numerator inside the Fourier transform and \tilde{v}_{trans} taking the place of \tilde{s} in the denominator.

In Fig. 10 we show the simulated amplitude of S_{11} as a function of frequency for the HERA dish and the PAPER element, observing a distinctive two peaked structure before a steep die off in delay that transitions to a shallower falloff at ≈ 150 ns. The first peak is due to the reflection of the input wave off of the back of the feed while the second, roughly 35 ns later arises from the transmitted component of the input wave reflecting off of the dish and arriving back at the feed. The ensuing long term die off arises from reflections within the feed and dish structure and for reasons that will be elaborated on in Patra et al. (in preparation) corresponds very closely to our simulations of the dish gain itself (compare with Fig. 6). We get a sense of the dynamic range of the measurement by unhooking the SMA adapter that attaches the sleeved dipole feed to the cable from our VNA, forming an open circuit that should ideally give a reflection coefficient of ≈ 1 at zero delay with no reflections at any other times. In this measurement, we find noise-like structure at ≈ -50 dB. Below ≈ 500 ns, we found that this structure does not integrate down with time, leading us to conclude that it is caused by systematics, likely uncalibrated low level reflections in the VNA-feed cables. The level of this noise sets the systematic floor in our measurements which we show as a grey shaded region in Fig. 10. We find that in the region where the S_{11} measurement is above the systematics floor, there is good agreement with our simulations (within several dB) and obeying the same trends as our simulation.

5. THE EFFECT OF THE HERA DISH CHROMATICITY ON FOREGROUND LEAKAGE AND SENSITIVITY

We are now in a position to explore the impact of the dish's performance on the leakage of foregrounds beyond the wedge, and into the EoR window. Beyond the delay kernels considered in this paper and Patra et al. (in preparation), the extent of leakage will depend both on the angular structure of the primary beam, which is established through measurements and simulations in

Neben et al. (2016) and the brightness of the foregrounds themselves. In this section, we investigate the amplitude of foreground leakage as a function of delay given the angular primary beam model and our simulation of the delay structure of the dish. We start by performing a physically motivated extrapolation of the delay structure observed in our simulations to cover the range of comoving scales relevant to power spectrum measurements (§ 5.1). In § 5.2, we combine this extrapolated delay response with simulations of foregrounds to determine the overall level of foreground power in HERA's visibilities. This leakage will cause large-scale LoS Fourier modes to be contaminated by foregrounds and hence inaccessible to the foreground filtering approach. Since the signal-to-noise ratio is maximized at the smallest k values, the loss of these modes will reduce the significance of the power spectrum detection and negatively impact the overall bottom line of the science that HERA can accomplish. We explore the impact of HERA's intrinsic beam chromaticity on science using the Fisher matrix formalism in § 5.3.

5.1. Extrapolating the Bandpass and Power Kernel

Our simulations of the Dish response only extend to ≈ 400 ns. However, interferometers are expected to be most sensitive to the 21 cm power spectrum at comoving scales between $k \approx 0.1 - 0.5\ h\text{Mpc}^{-1}$, corresponding to the delays between 180 and 900 ns at $z = 8$. To extrapolate out to the higher delays in this range, we assume that the response function is dominated by reflections between the feed and the dish. The long term falloff appears as a line on a linear-log plot (Fig. 6), indicating that the voltage response follows an exponential which we now show is indicative of reflections. We let Γ_d represent the reflection coefficient of the Dish vertex and Γ_f represent the reflection coefficient of the feed in the presence of each-other. An electromagnetic wave incident on the feed, at $t = 0$, is accepted with amplitude $(1 - \Gamma_f)$. The reflected component travels back to the dish and acquires an amplitude of $(\Gamma_f \Gamma_d)$ before returning at time, τ_d later where $(1 - \Gamma_f)$ will be accepted and Γ_f will be reflected back towards the dish. Summing the infinite series of reflections, the time dependent voltage at the feed is

$$\tilde{v}_r(t) = \sum_m (\Gamma_f \Gamma_d)^m \tilde{s}(t - m\tau_d), \quad (12)$$

which implies that

$$\tilde{r}_r(\tau) = \sum_m (\Gamma_f \Gamma_d)^m \delta_D(\tau - m\tau_d). \quad (13)$$

Since the number of reflections is $m = t/\tau_d$, than we can write the long-term delay response in discrete form as

$$\tilde{r}_n \approx (\Gamma_f \Gamma_d)^{nd\tau/\tau_d} \quad (14)$$

which is an exponential in time. We thus model our discrete voltage response as an exponential

$$\tilde{r} = AX^{(\tau/30\text{ns})} \quad (15)$$

to extrapolate beyond 400 ns by fitting for A and X in our simulations between 200 and 400 ns. In this pedagogical treatment, we have assumed that the reflection coefficients are frequency independent which is not the

case in real life. The impact of frequency dependent reflection coefficients is to replace the summands in equation 13 with the Fourier transform of $(\Gamma_f \Gamma_d)^m$ evaluated at $t = (\tau - m\tau_d)$. As long as $(\Gamma_f \Gamma_d)^m$ is compact in delay space, which is the case if the reflection coefficients evolve smoothly with frequency, then our pedagogical approximation still yields the power law in equation 15.

5.2. The Impact of the HERA Beam Chromaticity on Foreground Contamination

Given the HERA dish chromaticity, what Fourier modes will still be accessible with the delay filtering technique? To answer this question, we combine our extrapolated simulations of the HERA dish's spectral structure with simulations of foregrounds.

The foreground model is discussed in detail in Thyagarajan et al. (submitted) but we describe them briefly here for the readers convenience. It consists of two major components: diffuse synchrotron emission from our Galaxy whose structure is described by the Global Sky Model (GSM) of de Oliveira-Costa et al. (2008) and a population of point sources including objects from the NRAO Sky Survey (NVSS) (Condon et al. 1998) at 1.4 GHz and the Sydney University Molonglo Sky Survey (SUMMS) (Bock et al. 1999) at 843 MHz. Their fluxes are extrapolated to the observed 100-200 MHz band using a spectral index of $\langle\alpha\rangle = -0.83$ determined in Mauch et al. (2003). Visibilities are computed from the diffuse and point source models assuming an achromatic angular response for the HERA beam at 150 MHz described in Neben et al. (2016). We compute two sets of visibilities: one in which the spectral structure of the dish is assumed to be completely flat, and another in which the beam is multiplied by the frequency dependent gain at zenith determined by our simulations.

The foreground filtering procedure employed by PAPER and HERA involves delay transforming the visibilities and performing a 1d clean (Parsons & Backer 2009; Parsons et al. 2012) which discovers and subtracts foregrounds within the horizon plus a small buffer, allowing for the suppression of foreground side-lobes in delay space. The level of foreground subtraction possible by this procedure is limited by the thermal noise level on the visibility, which in turn depends on the number of time steps and redundant baselines that are averaged before performing the cleaning step. In this work, we assume that each visibility is cleaned independently with a twenty minute cadence. Each baseline is coherent for ≈ 10 s per night so this is equivalent to each local Sidereal time (LST) being integrated for ≈ 120 nights before cleaning. If we were to average over redundant baselines this number would drop enormously. The standard deviation on the real and imaginary part of a single delay transformed visibility is (Morales & Hewitt 2004)

$$\sigma_V = \frac{\sqrt{2B}k_B T_{sys}}{A_e \sqrt{\tau}}, \quad (16)$$

where A_e is the effective area of the dish, B is the bandwidth, T_{sys} is the system temperature, τ is the integration time, and k_B is the Boltzmann constant. For T_{sys} we use the equation $T_{sys} = 100\text{K} + T_{sky}$ where 100 K is the temperature of the PAPER receiver and $T_{sky} = 60(\lambda/1\text{ meter})^{2.55}$ is the sky temperature (Fixsen

et al. 2011). For A_e we use the value of 98 m^2 determined in Neben et al. (2016). We clean down to five times the thermal noise level. Subtracting a model of the sky is an alternative to cleaning but also assumes a priori knowledge of the foregrounds and the instrumental response. In Fig 11 we compare the delay transform of visibilities before and after cleaning at the LST of 4 hours. While cleaning is able to remove structure within the horizon, it does not reduce any of the power leaked outside of the horizon by the chromaticity of the dish. If we knew the spectral response of the dish perfectly, then we might be able to clean with this kernel and remove the supra-horizon structure. However, our design goal is for us to not require such precise instrumental knowledge (which would need to be less than one part in 10^{-4} to not be necessary).

To form estimates of the 21 cm power spectrum, we split each visibility into Blackman-Harris windowed subbands centered at redshift intervals of $\Delta z = 0.5$ and each with a power equivalent bandwidth of 10 MHz^{13} . The flat sky approximation allows us to Fourier transform each interval in frequency, square, and multiply by a set of prefactors to obtain a power spectrum estimate (Parsons et al. 2014),

$$\hat{P}(\mathbf{k}) = \left(\frac{2k_B}{\lambda^2}\right)^2 \frac{X^2 Y}{B_{pp} \Omega_{pp}} |\tilde{V}(\mathbf{u})|^2. \quad (17)$$

Here, λ is the central wavelength of the observation, k_B is the Boltzmann constant, B_{pp} is the integral of the square of the bandpass, and Ω_{pp} is the integral of the primary beam squared over solid angle. X and Y are linear factors converting between native interferometry and cosmological coordinates, defined through the relation $2\pi\mathbf{u} = 2\pi(u, v, \eta) = (Xk_x, Xk_y, Yk_z)$.

A drift scan instrument, HERA will observe the sky at many LSTs within the strip declination that passes through its primary beam, averaging over the power spectrum estimate at each LST. It is well documented that foreground power varies significantly over LST (Thyagarajan et al. 2015b), hence such an estimate will either filter or weight LSTs in a way that minimizes the impact of the most contaminated observations. For our analysis, we focus on a single LST of 4 hours which points out of the galactic plane and represents a relatively clean pointing similar to those we expect for HERA to concentrate its observing time on.

Computing the power spectra, we inspect the amplitude of foregrounds given the chromaticity and angular pattern of the HERA dish for baselines of two different lengths in Fig. 12. In both baselines, we find that the residuals after cleaning tend to be at similar levels except at the subband centered at $z = 8.5$ (150 MHz), in which foreground residuals remain above the signal level out to $k_{\parallel} = 0.23\text{ hMpc}^{-1}$. Several other baselines especially those oriented entirely in the E-W direction, which we do not show, contain up to two orders of magnitude greater galactic contamination as is noted in Thyagarajan et al. (2015a). In an analysis, these baselines would

¹³ The end to end width of each Fourier transformed interval is 20 MHz, however the power equivalent width of this interval (given by the integral of the bandpass squared) is only ≈ 0.5 the full width since the Blackman-Harris window suppresses the edge channels.

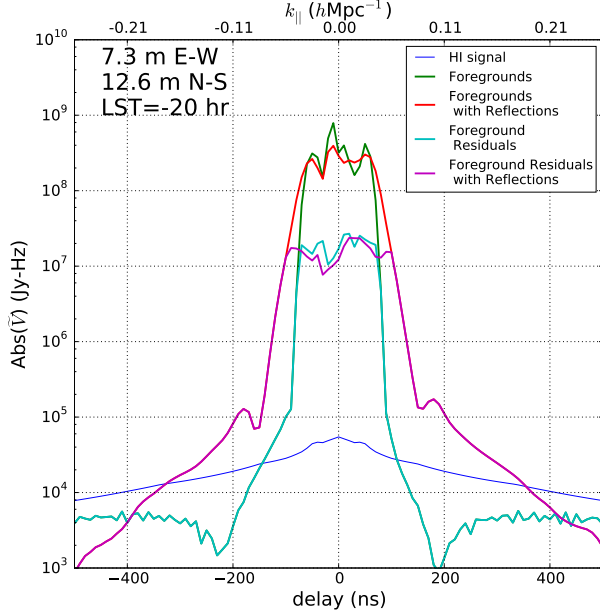


FIG. 11.— The absolute magnitude of a 100-200 MHz delay transformed visibility from a 14-meter baseline (blue line) compared to the same visibility (green line) contaminated by the reflections observed in our simulations of the HERA dish. We see that the extended delay kernel smooths out structure, originating from foregrounds, within the horizon. For HERA, we expect to use the delay-clean to remove foregrounds. However, the depth of cleaning is limited by the noise level on a single baseline (black line). We show the foreground residuals from a clean down to the 5σ noise level after 20 minutes of integration. Since cleaning cannot distinguish between foregrounds and signal, it should only be performed within a narrow region of delay-space, close to the horizon and cannot remove the broad wings leaked by the reflections unless they are accurately modeled.

be down-weighted or discarded so that they do not bias our final estimate.

The level of the foregrounds in Fig. 12 is conservative since no attempt has been made to apply inverse covariance weighting techniques (Tegmark 1997; Liu & Tegmark 2011; Dillon et al. 2013; Parsons et al. 2014; Liu et al. 2014a,b; Dillon et al. 2015c,b; Trott et al. 2016) or fringe rate filtering (Parsons et al. 2015). Applications of inverse covariance filters in recent PAPER observations have yielded reductions in foreground power by greater than an order of magnitude (Ali et al. 2015), hence our simulations show that even with the presence of beam chromaticity, HERA will be able to isolate foregrounds below the level of thermal noise in most of the EoR window.

5.3. The Implications of Dish Reflections on EoR Science

A primary near-term goal of 21 cm EoR observations is to obtain information about the nature of the sources that drove reionization. Since the amplitude of the 21 cm signal is maximal at smaller k values, a loss of large scale signal due to foreground contamination eliminates the modes that HERA would otherwise have the greatest signal to noise detections of, reducing its overall sensitivity. In this section, we use the Fisher Matrix formalism to estimate the impact of foreground leakage on HERA’s

sensitivity along with its ability to determine the astrophysics of reionization. The Fisher Matrix allows us to forecast the covariances and errors on reionization parameters given errors on power spectrum observations due to the uncertainties caused by cosmic variance and thermal noise which is in turn determined by the uv coverage and observing time of the interferometer. The covariance between the parameters, θ , of an astrophysical model is given by the inverse of the Fisher matrix, \mathbf{F} which for Gaussian and independently determined power spectrum bins may be written approximately as (Pober et al. 2014),

$$F_{ij} \approx \sum_{k,z} \frac{1}{\sigma^2(k,z)} \frac{\partial \Delta^2(k,z)}{\partial \theta_i} \frac{\partial \Delta^2(k,z)}{\partial \theta_j}, \quad (18)$$

where $\Delta^2(k,z)$ is the power spectrum amplitude for some $k-z$ bin and $\sigma^2(k,z)$ is the variance of the power spectrum estimate. We write this equation as approximate since it ignores additive terms arising from the dependence of $\sigma^2(k,z)$ on model parameters due to cosmic variance which only contribute at the $\approx 1\%$ level (Ewall-Wice et al. 2015).

To simulate Δ^2 , we use the publicly available 21cmFAST¹⁴ code (Mesinger et al. 2011) which generates realizations of the 21 cm brightness temperature field using the excursion set formalism of Furlanetto et al. (2004). We employ a popular three parameter model of reionization (Mesinger et al. 2012) with the following variables

- ζ : The “ionization efficiency” is defined in the Furlanetto et al. (2004) excursion formalism to be the inverse of the mass collapse fraction necessary to ionize a region and is computed from a number of other physical parameters including the fraction of collapsed baryons that form stars and the UV photon escape fraction. Because ζ acts as an efficiency parameter, its primary effect is to change the timing of reionization. We choose a fiducial value of $\zeta = 20$, though its possible values range anywhere between 5 and 50.
- R_{mfp} : The presence of Lyman limit systems and other potential absorbers within HII regions causes UV photons to have a finite mean free path denoted by R_{mfp} . In the 21cmFAST framework, HII regions cease to grow after reaching the radius of R_{mfp} , primarily impacting the morphology of the signal. We choose a fiducial value of $R_{\text{mfp}} = 15$ Mpc which is in line with recent simulations accounting for the subgrid physics of absorption (Sobacchi & Mesinger 2014).
- $T_{\text{vir}}^{\text{min}}$: The minimal mass of dark matter halos that hosted ionizing sources. While in principle, halos with virial temperatures as small as 10^2 K are thought to be able to form stars (Haiman et al. 1996; Tegmark et al. 1997), thermal and mechanical feedback have been seen to raise this limit to as high as 10^5 K (Springel & Hernquist 2003; Mesinger & Dijkstra 2008; Okamoto et al. 2008). We choose

¹⁴ http://homepage.sns.it/mesinger/DexM__21cmFAST.html

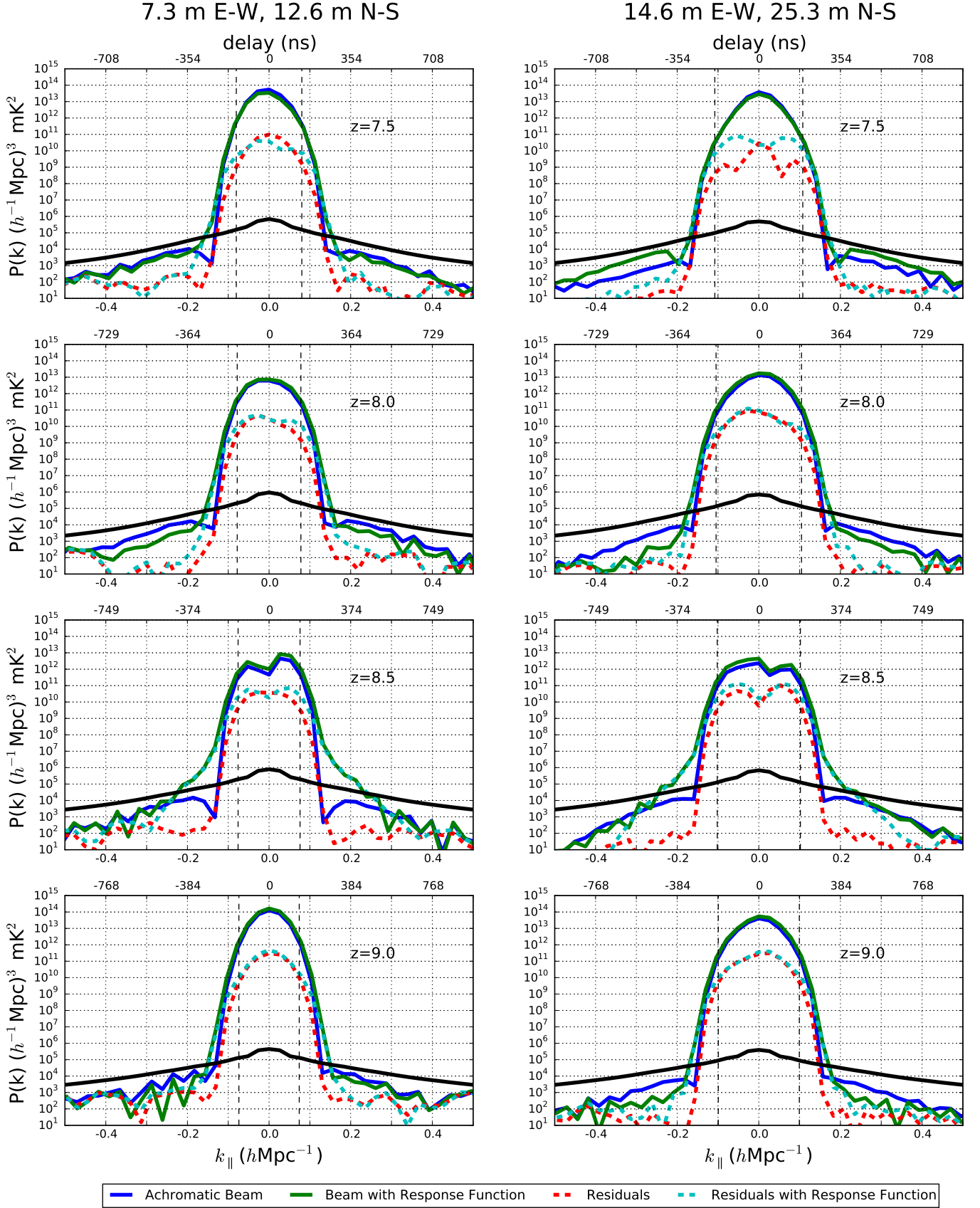


FIG. 12.— The delay transform power spectrum for different baselines over several redshifts with (green solid line) and without (blue solid line) the presence of the simulated chromaticity in the HERA dish. Each estimate is computed using the square of a Blackman-Harris windowed delay transform (equation 17) over a power equivalent bandwidth of 10 MHz. We also show the power spectra of foreground residuals after cleaning the entire 100 MHz band with (dashed cyan line) and without (red dashed line) the simulated spectral structure. For all subbands, except $z = 8.5$, we find that the reflections in the HERA dish have a negligible effect on the k_{\parallel} where the foregrounds drop below the signal level. This is the same subband where enhanced spectral structure due to reflections are observed in our simulations (Figs. 8 and 9).

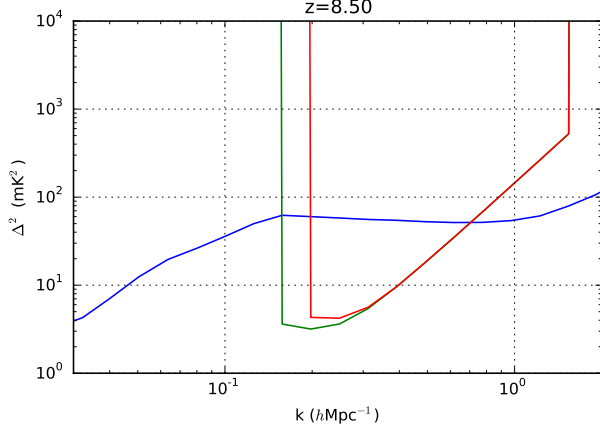


FIG. 13.— The 1σ thermal noise levels achieved by HERA-350 at redshift 8.5 with (red line) and without (green line) the presence of beam chromaticity due to the reflections studied in this work. We saw in Fig. 12 that with reflections, foregrounds exceed the signal level out to $k = 0.23 \text{ hMpc}^{-1}$ at $z = 8.5$ which we assume are unusable, forcing us to ignore modes out to 350 ns beyond the horizon, leading to the sensitivity projected in the red curve. The absence of these reflections allows us to work within 250 ns of the horizon (green curve), leading to an increase in sensitivity by a factor of ≈ 1.5 .

a fiducial value of $T_{\text{vir}}^{\text{min}} = 1.5 \times 10^4 \text{ K}$ which is set by the atomic line cooling threshold.

In order to account for the degeneracies in the power spectrum between heating from X-rays and reionization from UV photons, we also marginalize over three additional parameters that describe the impact of heating from early X-ray sources as explored in (Ewall-Wice et al. 2015). These are the X-ray heating efficiency, f_X ; the maximal energy of X-ray photons that are self absorbed by the ISM of early galaxies, ν_{min} ; and the spectral slope, α which are taken to have fiducial values of 1, 0.3 keV, and -1.2 respectively. We choose to parameterize our model in terms of the fractional difference of each variable from its fiducial value so that, for example, $\theta_\zeta = (\zeta - \zeta_{\text{fid}})/\zeta_{\text{fid}}$ and compute the derivatives in equation 18 by performing a linear fit to realizations of the 21 cm power spectrum calculated by 21cmFAST at $\theta_i = \pm 10^{-2}, \pm 5 \times 10^{-2}, \pm 10^{-1}$, and $\pm 2 \times 10^{-2}$.

For each measurement in the uv plane, the standard deviation of a power spectrum measurement ($\sigma^2(k, z)$) is given by the direct sum of sample variance and thermal noise (McQuinn et al. 2006) which in turn depends on the primary beam of the instrument and the time spent sampling each uv cell. For our analysis, we assume that the uv plane is sampled by circular apertures with effective areas of 98 m^2 and that $\tau(\mathbf{k})$ is determined by a drift scan in which non-instantaneously redundant baselines are combined within each uv cell. We compute the standard deviation of each (k, z) bin for the proposed 350-element deployment of HERA (HERA-350) using the public 21cmSense¹⁵ code (Pober et al. 2013b, 2014).

We have seen in Fig. 12 that the simulated chromaticity of the dish leaks foregrounds beyond the horizon to varying degrees depending on the subband with the worst leakage occurring at $z = 8.5$ centered at 150 MHz. In this subband, foregrounds exceed the signal out to $\sim 380 \text{ ns}$

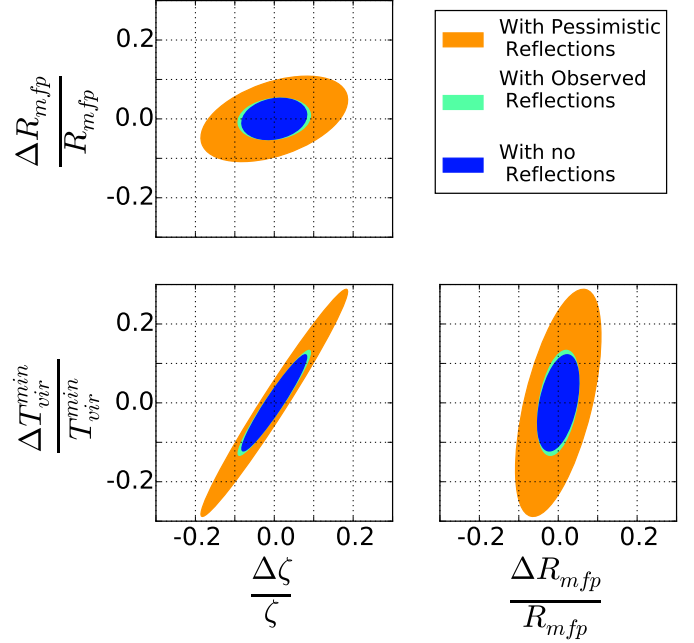


FIG. 14.— 95% confidence regions for reionization parameters assuming 1000 hours of observation on HERA-350 between the redshifts between 7.5 and 12. The presence of the reflections leads to an increase in the major axes of these confidence regions by a factor of one to two.

which for a 14.6 m baseline is $\approx 330 \text{ ns}$ beyond the horizon. At all other redshifts, the leakage due to beam chromaticity only extends to $\approx 250 \text{ ns}$ beyond the horizon. To determine the impact of our observed beam chromaticity on HERA's ability to constrain the astrophysics of reionization, we consider three different scenarios for beam chromaticity that capture a range of possibilities informed by our simulations.

- **Optimistic: The observed reflections are an artifact of the simulation.** It is possible that the long term reflections observed in the center of our gain are artifacts of our modeling. Dissipative effects due to unmodeled non-idealities in the geometry of the dish may allow reflected radio waves to be better absorbed or escape into space. In our most optimistic scenario, we assume their absence in which case the foregrounds pass below the level of the signal at 250 ns beyond the horizon at all redshifts between $z = 7$ and 12, consistent with what is observed in the bands where the dish chromaticity is less severe or when it is not present at all. We do not consider the possibility that optimal inverse covariance weighting of the foregrounds may actually decrease the minimal delays accessible to below the 250 ns above the horizon observed in our simulations. Hence, this scenario is actually somewhat conservative and certainly more pessimistic than previous Fisher analyses Pober et al. (2014); Liu et al. (2015); Liu & Parsons (2016); Ewall-Wice et al. (2015).

- **Moderate: The Simulations accurately capture the chromaticity of the dish.** In this case, we assume that the reflections cause foregrounds to pass below the level of the signal at 250 ns beyond

¹⁵ <https://github.com/jpober/21cmSense>

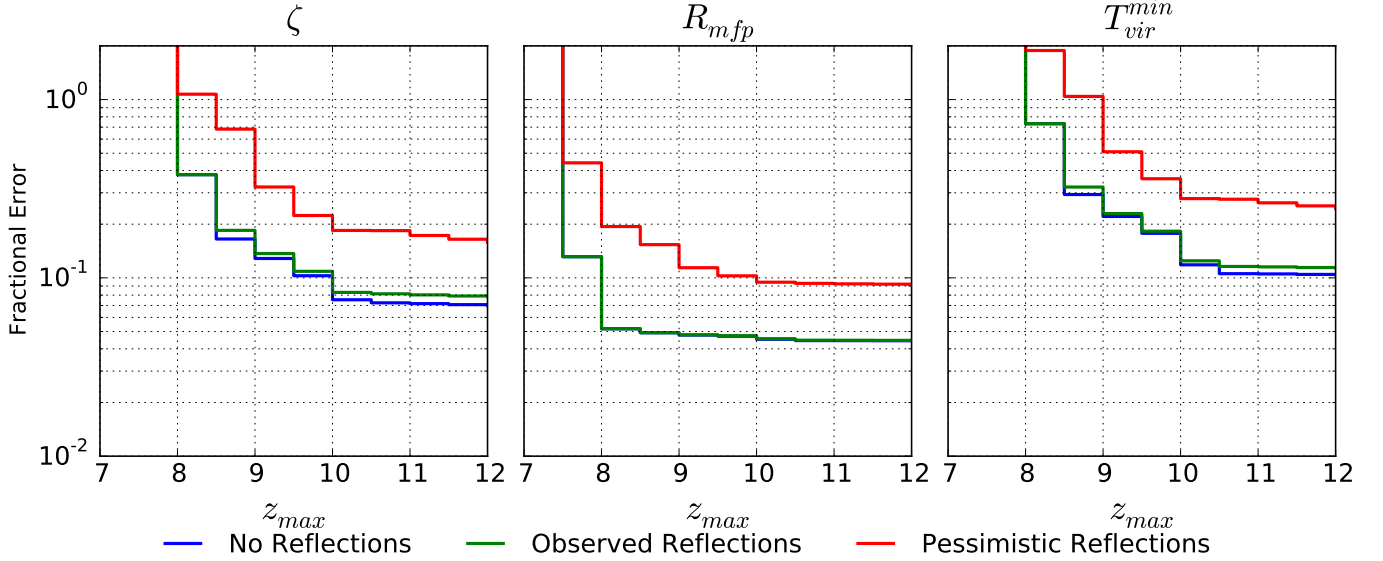


FIG. 15.— Fractional Errors on reionization and heating parameters as a function of maximal observed redshift out to the low end of HERA-350’s initial observing band at $z = 12$. The presence of strong reflections contained within a small subband at $z = 8.5$ has a minimal impact on our overall constraints on reionization parameters. If these reflections are not localized they can worsen our sensitivity to some parameters such as $T_{\text{vir}}^{\text{min}}$ by a factor of two.

the horizon except at redshift 8.5 where they pass below the foregrounds at 350 ns beyond the horizon.

- **Pessimistic: The reflections are present in all sub-bands.** In this scenario, we assume that the spectral structure observed in the neighborhood of 150 MHz is present throughout the entire 100–200 MHz frequency range covered by HERA. We decide to include this more pessimistic scenario since our simulations and measurements are run with a termination impedance of $\approx 100 - 125 \Omega$ which is actually a better match to the feed at the edges of the 100 – 200 MHz band, reflecting 1 – 3% power at the edges while reflecting $\approx 10\%$ power at 150 MHz. In an actual cosmological measurement, the feed is terminated by an LNA whose impedance may not be perfectly matched at all frequencies despite the best efforts of its designers, hence it is possible that we will find the reflections across the entirety of the 100 MHz band.

In Fig. 13, we compare the level of 1σ thermal noise for our optimistic and moderate scenarios at $z = 8.5$ to the amplitude of the 21 cm signal. The smallest k modes lost to foreground contamination are the highest signal to noise measurements that HERA is expected to obtain. Their absence impacts sensitivity in two ways. By leading to a reduction in the maximal signal to noise ratio of ≈ 1.5 and a reduction in the total number of modes that the instrument is able to measure.

Folding our calculations of thermal noise and the derivatives of Δ^2 into equation 18 and inverting, we obtain the covariance matrix for model parameters. We show the 95% confidence ellipses for the reionization parameters in Fig. 14. The presence of reflections within a limited sub-band about $z = 8.5$ leads to an almost negligible increase in the extent of our confidence intervals while the presence of the reflections across the entire band causes the lengths and widths of our confidence

ellipses to increase by a factor of ≈ 2 . The diagonal elements of our covariance give us error bars on each parameter which we plot in Fig. 15. We see that similar to our confidence regions, the error bars on reionization parameters for our optimistic and moderate scenarios are nearly indistinguishable. In our worst case where reflections of a similar level as observed in the middle of our band are present everywhere, we see an increase in our error bars by a factor of ≈ 2 .

The error bars on reionization parameters, even for our most optimistic model, are a factor of a few larger than the “moderate” errors predicted in previous works using likelihood analyses such as Pober et al. (2014), Greig & Mesinger (2015); Greig et al. (2015b,a) Ewall-Wice et al. (2015), Liu et al. (2015); Liu & Parsons (2016). There are several reasons for this. Firstly, in our most optimistic scenario, we assumed that foregrounds cause the signal to be inaccessible below 250 ns beyond the edge of the wedge which corresponds to $k_{\text{min}} \approx 0.15 \text{ hMpc}^{-1}$ at $z = 8.5$ while in previous works a minimal comoving $k_{\text{min}} \approx 0.1 \text{ hMpc}^{-1}$ was used. Secondly, previous studies assumed a fully illuminated HERA aperture, which for a 14 m diameter dish predicts an effective area of $\approx 155 \text{ m}^2$. Electromagnetic simulations and ORBCOMM mapping of the angular beam pattern of the HERA dish show that the effective area of the antenna element is actually $\approx 98 \text{ m}^2$ at 137 MHz which leads to an increase in the overall thermal noise levels by a factor of ≈ 1.5 (Neben et al. 2016).

Although conservative, our analysis shows that the level of chromaticity present in the HERA beams is not yet an insurmountable obstacle for the 21 cm power spectrum measurement. Even with the additional systematics introduced by the reflections in the Dish geometry, the array will still obtain a $\gtrsim 10\sigma$ detection of the power spectrum and be capable of establishing precision constraints on the properties of the sources that reionized the IGM.

6. CONCLUSIONS

In this paper, we have formally described the impact of instrumental chromaticity on foreground contamination of the 21 cm signal. We have also used simulations of electromagnetic waves incident from zenith on the primary antenna element on HERA to determine the extent to which reflections and other frequency dependent structure in the dish leak foregrounds into the EoR window. The results of our simulations of the dish's voltage response are broadly consistent with reflectometry measurements (Patra et al. in preparation) and can be summarized in the following points.

- The 14-m dish and inverted dipole feed configuration introduces reflections and, as a result, spectral structure, that is in excess of that observed in the antenna design for HERA's predecessor, PAPER. The dish design is intended to greatly increase array collecting area over PAPER without significantly raising the number of correlated elements while narrowing the angular field of view and suppressing the overall amplitude of foregrounds. We find that in achieving these ends, some degree of spectral smoothness has been sacrificed. Because foreground filtering in delay space cannot distinguish between signal and foregrounds, any regions of k -space contaminated by these reflections are effectively unusable in a 21 cm measurement unless they can be modeled to high fidelity and removed.
- These reflections appear to be contained within the central 10 MHz of the HERA band. This is likely due to a better impedance match at the band edges between the feed and the terminals which may not exist in an actual deployment. It is also possible that the non-ideal properties of an actual antenna will allow these reflections to escape the dish after a short time or be dissipated, rather than reflecting continually to long delays. Because estimates of the power spectrum are obtained from sub-intervals of ≈ 10 MHz, the reflections that we have simulated will only impact a single $\Delta z = 0.5$ redshift interval.
- Simulating the impact of these reflections on foreground leakage using the foreground model of Thyagarajan et al. (submitted), we find that the beam chromaticity extends foregrounds above the

level of the cosmological signal to ≈ 350 ns beyond the horizon while without the reflections, foregrounds extend above the signal to ≈ 250 ns beyond the horizon. These forecasts are conservative in that we do not attempt to inversely weight the foregrounds by their covariances, nor have mitigation algorithms such as delay rate filtering been applied.

- If the reflections are contained within a 10 MHz subband around 150 MHz, then the overall constraints that HERA will be able to place on the astrophysics of reionization are minimally impacted. The feed design is well matched near the band edges to the termination impedances in both our measurements and simulations which may not be the case in the field, hence we consider it a realistic possibility that these reflections contaminate the entire band. If this is the case, our constraints on reionization parameters will suffer a two-fold increase in uncertainty but still remain on the order of 10%. Measuring the global properties of the sources that reionized the universe to this accuracy will be an unprecedented accomplishment.

Our results are very encouraging since they show that the HERA design is capable of isolating the foregrounds to sufficiently low delays to make a high significance detection of the 21 cm power spectrum during the EoR. They also emphasize the importance of mitigating spectral structure in the analogue signal chain. The reflections masking our signal at $k = 0.2 h\text{Mpc}^{-1}$ are at the level of one part in 10^{-4} and are mathematically identical to Fourier modes introduced by any instrumental spectral structure and the requirement that spectral structure be smaller than 10^{-4} dB at ≈ 350 ns to be below the signal is applicable to all steps in the signal chain beyond the dish. A full statement of such a specifications for spectral structure to observe the EoR power spectrum at different k values will be given in Thyagarajan et al. (submitted). Hence any interferometer designed for EoR observing should ensure that such structure is absent from the signal chain at the $\sim 10^{-5}$ level or less at ≈ 350 ns or be absolutely certain that their calibration strategy can faithfully remove this structure without introducing any spurious, frequency-dependent artifacts at or above this level due to foreground mismodeling or thermal noise.

REFERENCES

- Ali, Z. S., et al. 2015, *ApJ*, 809, 61
 Barry, N., et al. in preparation
 Beardsley et al. in preparation
 Bernardi, G., McQuinn, M., & Greenhill, L. J. 2015, *ApJ*, 799, 90
 Bernardi, G., et al. 2009, *A&A*, 500, 965
 Bock, D. C.-J., Large, M. I., & Sadler, E. M. 1999, *AJ*, 117, 1578
 Bowman, J. D., & Rogers, A. E. E. 2010, *Nature*, 468, 796
 Burns, J. O., et al. 2012, *Advances in Space Research*, 49, 433
 Colegate, T. M., et al. 2015, *ArXiv e-prints*
 Condon, J. J., Cotton, W. D., Greisen, E. W., Yin, Q. F., Perley, R. A., Taylor, G. B., & Broderick, J. J. 1998, *AJ*, 115, 1693
 Datta, A., Bowman, J. D., & Carilli, C. L. 2010, *ApJ*, 724, 526
 de Oliveira-Costa, A., Tegmark, M., Gaensler, B. M., Jonas, J., Landecker, T. L., & Reich, P. 2008, *MNRAS*, 388, 247
 DeBoer, D., et al. submitted
 Dillon, J. S., Liu, A., & Tegmark, M. 2013, *Phys. Rev. D*, 87, 043005
 Dillon, J. S., et al. 2014, *Phys. Rev. D*, 89, 023002
 —. 2015a, *Phys. Rev. D*, 91, 123011
 —. 2015b, *Phys. Rev. D*, 91, 123011
 —. 2015c, *Phys. Rev. D*, 91, 023002
 Ewall-Wice, A., Hewitt, J., Mesinger, A., Dillon, J. S., Liu, A., & Poher, J. 2015, *ArXiv e-prints*
 Ewall-Wice, A., et al. in review, Submitted to *MNRAS*
 Fixsen, D. J., et al. 2011, *ApJ*, 734, 5
 Furlanetto, S. R., Oh, S. P., & Briggs, F. H. 2006, *Phys. Rep.*, 433, 181
 Furlanetto, S. R., Zaldarriaga, M., & Hernquist, L. 2004, *ApJ*, 613, 1
 Greenhill, L. J., & Bernardi, G. 2012, *ArXiv e-prints*
 Greig, B., & Mesinger, A. 2015, *MNRAS*, 449, 4246

- Greig, B., Mesinger, A., & Koopmans, L. V. E. 2015a, ArXiv e-prints
- Greig, B., Mesinger, A., & Pober, J. C. 2015b, ArXiv e-prints
- Haiman, Z., Thoul, A. A., & Loeb, A. 1996, ApJ, 464, 523
- Jacobs, D., et al. in preparation
- Jacobs, D. C., et al. 2015, ApJ, 801, 51
- Liu, A., & Parsons, A. R. 2016, MNRAS, 457, 1864
- Liu, A., Parsons, A. R., & Trott, C. M. 2014a, Phys. Rev. D, 90, 023018
- . 2014b, Phys. Rev. D, 90, 023019
- Liu, A., Pritchard, J. R., Allison, R., Parsons, A. R., Seljak, U., & Sherwin, B. D. 2015, ArXiv e-prints
- Liu, A., & Tegmark, M. 2011, Phys. Rev. D, 83, 103006
- Liu, A., Tegmark, M., Morrison, S., Lutomirski, A., & Zaldarriaga, M. 2010, MNRAS, 408, 1029
- Mauch, T., Murphy, T., Buttery, H. J., Curran, J., Hunstead, R. W., Piestrzynski, B., Robertson, J. G., & Sadler, E. M. 2003, MNRAS, 342, 1117
- McQuinn, M., Zahn, O., Zaldarriaga, M., Hernquist, L., & Furlanetto, S. R. 2006, ApJ, 653, 815
- Mesinger, A., & Dijkstra, M. 2008, MNRAS, 390, 1071
- Mesinger, A., Furlanetto, S., & Cen, R. 2011, MNRAS, 411, 955
- Mesinger, A., McQuinn, M., & Spergel, D. N. 2012, MNRAS, 422, 1403
- Morales, M. F., Hazelton, B., Sullivan, I., & Beardsley, A. 2012, ApJ, 752, 137
- Morales, M. F., & Hewitt, J. 2004, ApJ, 615, 7
- Morales, M. F., & Wyithe, J. S. B. 2010, ARA&A, 48, 127
- Neben, A. R., et al. 2015, Radio Science, 50, 614
- . 2016, ArXiv e-prints
- Okamoto, T., Gao, L., & Theuns, T. 2008, MNRAS, 390, 920
- Paciga, G., et al. 2013, MNRAS, 433, 639
- Parsons, A. R., & Backer, D. C. 2009, AJ, 138, 219
- Parsons, A. R., Liu, A., Ali, Z. S., & Cheng, C. 2015, ArXiv e-prints
- Parsons, A. R., Pober, J. C., Aguirre, J. E., Carilli, C. L., Jacobs, D. C., & Moore, D. F. 2012, ApJ, 756, 165
- Parsons, A. R., et al. 2010, AJ, 139, 1468
- . 2014, ApJ, 788, 106
- Patra et al. in preparation, ApJ
- Pober, J. C., et al. 2012, AJ, 143, 53
- . 2013a, ApJ, 768, L36
- . 2013b, AJ, 145, 65
- . 2014, ApJ, 782, 66
- . 2015, ApJ, 809, 62
- . 2016, ArXiv e-prints
- Pritchard, J. R., & Loeb, A. 2012, Reports on Progress in Physics, 75, 086901
- Sobacchi, E., & Mesinger, A. 2014, MNRAS, 440, 1662
- Sokolowski, M., et al. 2015, PASA, 32, 4
- Springel, V., & Hernquist, L. 2003, MNRAS, 339, 312
- Tegmark, M. 1997, Phys. Rev. D, 55, 5895
- Tegmark, M., Silk, J., Rees, M. J., Blanchard, A., Abel, T., & Palla, F. 1997, ApJ, 474, 1
- Thompson, A. R., Moran, J. M., & Swenson, G. W. 1986, Interferometry and synthesis in radio astronomy
- Thyagarajan, N., Helfand, D. J., White, R. L., & Becker, R. H. 2011, ApJ, 742, 49
- Thyagarajan, N., et al. 2013, ApJ, 776, 6
- . 2015a, ApJ, 807, L28
- . 2015b, ApJ, 804, 14
- Thyagarajan et al. submitted, ApJ
- Tingay, S. J., et al. 2013, PASA, 30, 7
- Trott, C. M., et al. 2016, ArXiv e-prints
- van Haarlem, M. P., et al. 2013, A&A, 556, A2
- Vedantham, H., Udaya Shankar, N., & Subrahmanyam, R. 2012, ApJ, 745, 176
- Voytek, T. C., Natarajan, A., Jáuregui García, J. M., Peterson, J. B., & López-Cruz, O. 2014, ApJ, 782, L9
- Wieringa, M. H. 1992, Experimental Astronomy, 2, 203
- Zaldarriaga, M., Furlanetto, S. R., & Hernquist, L. 2004, ApJ, 608, 622
- Zheng, H., et al. 2013, ArXiv e-prints
- . 2014, MNRAS, 445, 1084